



# Self-reconstruction of paddle-wheel copper-node to facilitate the photocatalytic CO<sub>2</sub> reduction to ethane

Shijie Xie<sup>a,b,1</sup>, Yangfan Li<sup>a,b,1</sup>, Bo Sheng<sup>a,b</sup>, Wanyi Zhang<sup>a,b</sup>, Wei Wang<sup>a</sup>, Chuncheng Chen<sup>a,b</sup>, Jikun Li<sup>a,\*</sup>, Hua Sheng<sup>a,b,\*</sup>, Jincai Zhao<sup>a,b</sup>

<sup>a</sup> Key Laboratory of Photochemistry, Institute of Chemistry Chinese Academy of Sciences, Beijing National Laboratory for Molecular Sciences, Beijing 100190, PR China

<sup>b</sup> University of Chinese Academy of Sciences, Beijing 100049, PR China

## ARTICLE INFO

### Keywords:

Carbon dioxide fixation  
Photocatalysis  
Metal-organic framework  
Reconstruction  
Hydrocarbons

## ABSTRACT

Obtaining high-value-added products like C<sub>2+</sub> hydrocarbons from CO<sub>2</sub> reduction in a photocatalytic system has always remained a great challenge. Herein we fabricated a  $\pi$ - $\pi$  stacking hybrid photocatalyst by combining two two-dimensional (2D) materials of g-C<sub>3</sub>N<sub>4</sub> and Cu-porphyrin metal-organic framework (MOF). This hybrid photocatalyst exhibited the excellent capability to reduce CO<sub>2</sub> into C<sub>2</sub>H<sub>6</sub> in a selectivity of 44% and the selectivity of total hydrocarbons (C<sub>2</sub>H<sub>6</sub> and CH<sub>4</sub>) was as high as 71%, as one of the best performances among the reported photocatalytic systems. The node sites of 2D-MOF were identified to be critical for the generation of C<sub>2</sub>H<sub>6</sub>, and a self-reconstruction during photocatalysis was clarified: the initial paddle-wheel Cu<sup>II</sup><sub>2</sub>(COO)<sub>4</sub> node was reconstructed to the partially reduced Cu<sup>I+δ</sup><sub>2</sub>(COO)<sub>3</sub>. Such reconstruction strengthened the trapping of in-situ generated CO and the synergistic action of the dual-Cu-site, therefore, achieved the efficient C-C coupling to form C<sub>2</sub>H<sub>6</sub>.

## 1. Introduction

The excessive emission of carbon dioxide has been recognized as one of the major causes of global climate change and therefore aroused widespread attentions [1–3]. By imitating the natural photosynthesis process, the artificial photosynthesis [4] that photocatalytically converts CO<sub>2</sub> to high-value-added carbon products as CO [5,6], formic acid [7], ethanol [8,9] or hydrocarbons [10,11] with solar light as driving force would be a promising strategy to accelerate the carbon cycling and address the issue of the excessive atmospheric CO<sub>2</sub>. However, suffered from the limited separation efficiency of photogenerated carriers [12, 13] and the consequent low electron densities contributing to CO<sub>2</sub> reduction, [14] the current CO<sub>2</sub> reduction products in a photocatalytic system are mainly restricted to the two-electron reduced primary product of CO, [15,16] while the evolutions of highly reduced hydrocarbons, especially the C-C coupling products (i.e. ethane or ethylene) via a kinetically sluggish multielectron process are seldomly reported [17–19]. Therefore, great efforts have been devoted to searching for the

photocatalyst that can efficiently reduce CO<sub>2</sub> to hydrocarbons beyond CO.

Since the direct one-electron reduction of nonpolar CO<sub>2</sub> to CO<sub>2</sub><sup>•−</sup> requires a huge reductive potential of around −1.9 V (vs NHE), [20,21] the trapping and activation of the linear CO<sub>2</sub> molecules on the surface sites of the catalyst are necessary to lower down the reaction barrier, [22–24] and in most cases, it is the *d*-electron donation from the transition-metal site to the  $\pi$  antibonding orbital of CO<sub>2</sub> that weakens the C=O bonds and bends the CO<sub>2</sub> molecular [22,25]. Therefore, the type of metal and its coordination circumstance that determine the localized *d*-electron density should be of great significance for the CO<sub>2</sub> activation and the further reduction [26,27]. As a new type of catalyst constructed by the highly conjunctive organic framework and the embedded metal sites in the framework, the metal-organic frameworks (MOF) based materials have been recently applied in electrochemical or photocatalytic CO<sub>2</sub> reduction [10,28,29]. Owing to the varied building blocks of metal nodes and organic ligand, MOF contains metal sites with distinctive coordination atmosphere, either the metal-oxygen clusters in

\* Corresponding author.

\* Corresponding author at: Key Laboratory of Photochemistry, Institute of Chemistry Chinese Academy of Sciences, Beijing National Laboratory for Molecular Sciences, Beijing 100190, PR China.

E-mail addresses: [jikunli@iccas.ac.cn](mailto:jikunli@iccas.ac.cn) (J. Li), [hsheng@iccas.ac.cn](mailto:hsheng@iccas.ac.cn) (H. Sheng).

<sup>1</sup> Authors made equal contributions.

the nodes or the single-site metal coordinated in the organic ligands. Such construction manner of MOF makes it a huge pool of transition-metal sites under varied coordination circumstances, which becomes promising in search of high-efficient CO<sub>2</sub> reduction catalyst as well as the mechanistic studies of the structure-function relationship.

For one of most explored MOF materials, the metal-porphyrin based MOF (PMOF), it has been well recognized that the type of the N-coordinated metal site in porphyrin ring (MN<sub>4</sub>) significantly affects the efficiency and selectivity of CO<sub>2</sub> reduction: e.g., Jiang et al. demonstrated the alternation in the valence state of cobalt from Co<sup>II</sup> to Co<sup>III</sup> in Co-PMOF switched the selectivity of CO<sub>2</sub> reduction towards formic acid, [30] while Wang et al. uncovered that when MN<sub>4</sub> was occupied by Cu rather than Au, the generation of CH<sub>4</sub> was more favored [31]. However, much less attention has been focused on another type of metal site, the metal node, which is usually the carboxylate-coordinated metal-oxygen clusters (M<sub>x</sub>(COO)<sub>y</sub>). Compared with MN<sub>4</sub>, M<sub>x</sub>(COO)<sub>y</sub> contains more metal atoms, and since the O-coordination is weaker than N-coordination, the structure of M<sub>x</sub>(COO)<sub>y</sub> would be more dynamically switchable during the catalytic reactions [32–34]. These together makes the mechanism of the CO<sub>2</sub> reduction on metal node more complicated, and the investigation is therefore more challenging. But an intriguing aspect of CO<sub>2</sub> reduction on M<sub>x</sub>(COO)<sub>y</sub> is that compared with MN<sub>4</sub> of single-site feature, the node (M<sub>x</sub>(COO)<sub>y</sub>) consist of several adjacent metal sites should act with CO<sub>2</sub> molecules in a quite different manner, especially when considering that the CO<sub>2</sub> reduction to C-C coupling hydrocarbons requires the collaboration of multiple reaction sites and multiple electrons [35]. In addition, the actual electron density of photoelectrons involved in the catalytic reaction is relatively small due to the low separation efficiency of photogenerated carriers in single-component semiconductors, which is not favored in multi-electron reduction of CO<sub>2</sub> to C-C coupling hydrocarbons. So, the MOF alone may not meet that need, and another semiconductor such as graphitic carbon nitride (g-C<sub>3</sub>N<sub>4</sub>) severing as the electron pool is employed. Recently, g-C<sub>3</sub>N<sub>4</sub> as a kind of semiconductor with a graphene-like layered structure and a suitable band position capable of CO<sub>2</sub> reduction is receiving more and more attention [36,37]. The ultrathin nature of g-C<sub>3</sub>N<sub>4</sub> makes it easy to hybrid with two-dimensional (2D) MOF by  $\pi$ - $\pi$  stacking to form heterojunction to facilitate the photoelectron from g-C<sub>3</sub>N<sub>4</sub> flow into MOF, which addresses the problem of electron-hole recombination and lacking of active sites of g-C<sub>3</sub>N<sub>4</sub> and providing extra electrons to MOF [38].

Herein, two-dimensional (2D) porphyrin MOF with tetrakis (4-carboxylphenyl) porphyrin (TCPP) as building blocks was used as a model to uncover the roles of distinct metal sites in photocatalytic CO<sub>2</sub> reduction. A series of 2D-MOF was fabricated, nominating as M<sub>a</sub>-M<sub>b</sub>TCPP. As the structure is shown in Fig. 1d, M<sub>a</sub> represents the carboxylate-coordinated metal nodes of (M<sub>a</sub>)<sub>2</sub>(COO)<sub>4</sub> in a paddle-wheel structure while M<sub>b</sub> stands for the M<sub>b</sub>N<sub>4</sub> in the center of the porphyrin ring. A  $\pi$ - $\pi$  stacking heterojunction of g-C<sub>3</sub>N<sub>4</sub>/M<sub>a</sub>-M<sub>b</sub>TCPP was further established. Upon illumination, g-C<sub>3</sub>N<sub>4</sub> with a conduction band potential around  $-1.3$  V (vs. NHE) affords a strong driving force for reduction reactions and to provide electrons in the hybrid catalyst. On the hybrid catalyst of g-C<sub>3</sub>N<sub>4</sub>/Cu-CuTCPP, the photocatalytic CO<sub>2</sub> reduction beyond CO was achieved with 44% selectivity of C<sub>2</sub>H<sub>6</sub> and 27% of CH<sub>4</sub> as the major hydrocarbon products. Furthermore, with Cu in the M<sub>b</sub>N<sub>4</sub> site unchanged, the alternation of the metal node (M<sub>a</sub>)<sub>2</sub>(COO)<sub>4</sub> from Cu to Zn leads to the significantly suppressed C<sub>2</sub>H<sub>6</sub>/CH<sub>4</sub> generation, suggesting the irreplaceable role of the Cu<sub>2</sub>(COO)<sub>4</sub> node in the formation of C-C coupling hydrocarbons. More intriguingly, based on X-ray absorption fine structure (XAFS) and electron paramagnetic resonance (EPR) analysis, it is consolidated that a structural reconstruction of the Cu-node has proceeded during the photocatalytic reactions: by accepting the photogenerated electrons from g-C<sub>3</sub>N<sub>4</sub>, the initial Cu<sup>II</sup><sub>2</sub>(COO)<sub>4</sub> node is partly reduced to Cu<sup>I+ $\delta$</sup> <sub>2</sub>(COO)<sub>3</sub> with decreased O-coordination numbers and shortened Cu-Cu distance. In the reconstructed Cu-node, the reduction of Cu<sup>II</sup> to Cu<sup>I+ $\delta$</sup>  facilitates the trapping of the in-situ generated CO molecules, while the coordinatively unsaturated

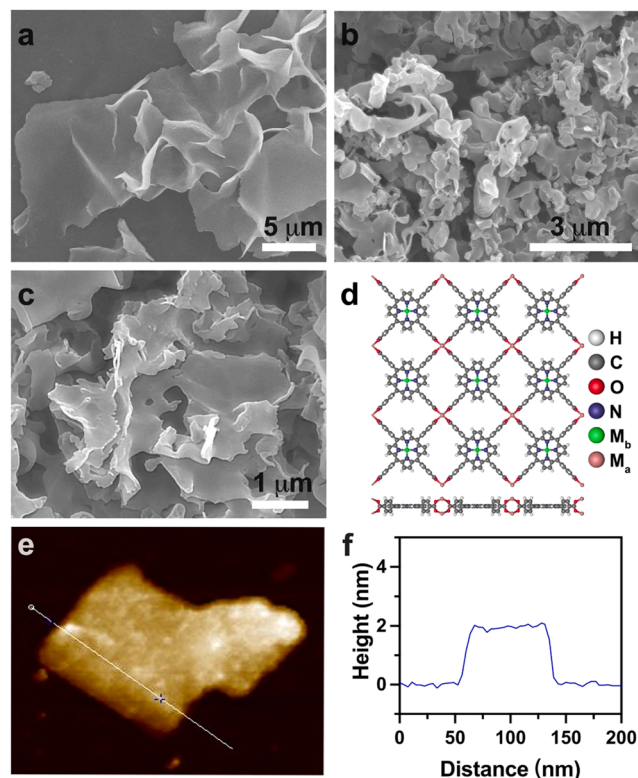


Fig. 1. SEM images of a) Cu-CuTCPP MOF, b) g-C<sub>3</sub>N<sub>4</sub>, and c) hybridized g-C<sub>3</sub>N<sub>4</sub> and Cu-CuTCPP. d) The scheme for the structure of M<sub>a</sub>-M<sub>b</sub>TCPP MOF. e) AFM image and f) corresponding height profiles of Cu-CuTCPP MOF.

structure favors the synergistic C-C coupling reaction on the dual-site Cu, leading to a significantly enhanced generation of C<sub>2</sub>H<sub>6</sub> multielectron-reduced products.

## 2. Experimental section

### 2.1. Materials

4,4,4,4-(Porphine-5,10,15,20-tetrayl) tetrakis (benzoic acid) (TCPP) was purchased from Alfa Aesar. Copper (II) nitrate hemi(pentahydrate), benzoic acid, zinc nitrate, and urine were obtained from Inno-Chem. Nafion D-521 dispersion (5% w/w in water and 1-propanol) was purchased from Alfa Aesar. Triethylamine (TEA) was purchased from Sigma-Aldrich. All the chemicals are analytical grade and used without further purification. Deionized water was prepared with a Milli-Q purification system and used throughout all the experiments.

### 2.2. Synthesis

#### 2.2.1. Synthesis of Cu-CuTCPP and Zn-ZnTCPP MOF nanosheets

In a typical synthetic procedure of Cu-CuTCPP MOF sheets, 20 mg TCPP and 45 mg Cu<sub>2</sub>(NO<sub>3</sub>)<sub>4</sub>·5H<sub>2</sub>O were dispersed in the mixed solvents of 60 mL *N,N*-dimethylformamide (DMF) and 5 mL water in a 100 mL round-bottom flask. Subsequently, 1.8 g benzoic acid was added into the solution. The mixture was heated to 90 °C and kept for 4 h under stirring. After centrifugation and washing with ethanol several times, the as-prepared Cu-CuTCPP MOF was dried under evacuation overnight. The synthesis of Zn-ZnTCPP MOF was under identical conditions except for the use of Zn(NO<sub>3</sub>)<sub>2</sub> instead of Cu(NO<sub>3</sub>)<sub>2</sub>.

#### 2.2.2. Synthesis of Zn-CuTCPP MOF nanosheets

To synthesize 2D-MOF containing mixed types of metals, the copper (II) complex of meso-tetra(4-carboxyphenyl) porphyrin (CuTCPP) was

first prepared. 0.33 mmol TCPP and 1.82 mmol  $\text{CuCl}_2$  were refluxed in DMF for 2 h, then the as-synthesized CuTCPP was precipitated from the solution by adding excessive water. Then the synthesis of Zn-CuTCPP was started from 28 mg CuTCPP and 35 mg  $\text{Zn}(\text{NO}_3)_2$ , and the detailed reaction conditions were identical to the above 2D-MOF with a single type of metal.

### 2.2.3. Synthesis of g- $\text{C}_3\text{N}_4$ nanosheets

To obtain the g- $\text{C}_3\text{N}_4$  nanosheet, urine (5.0 g) was placed in an open ceramic crucible and heated to 550 °C at a ramp of 2 °C·min<sup>-1</sup>. The aerobic calcination of the precursors at 550 °C was sustained for 2, 4, 6, and 8 h, respectively, to search for the optimal calcination time for the formation of thin nanosheet morphology. As shown in the XRD patterns in Fig. S1b, the prolonged calcination resulted in the reduced thickness of g- $\text{C}_3\text{N}_4$  nanosheets, as indicated by the decreased peak intensity at 27.4°. Therefore, under the optimal 8 h calcination, the thinnest g- $\text{C}_3\text{N}_4$  nanosheet with a thickness around 5 nm in light yellow color was obtained (Fig. S1c and d, Supporting Information, SI), which was employed for the further fabrication of heterojunctions.

### 2.2.4. Fabrication of 2D/2D heterojunction by g- $\text{C}_3\text{N}_4$ and $\text{M}_a\text{-M}_b\text{TCPP MOF}$

The hybridization of g- $\text{C}_3\text{N}_4$  and  $\text{M}_a\text{-M}_b\text{TCPP MOF}$  (Cu-CuTCPP, Zn-CuTCPP, and Zn-ZnTCPP) included two main steps. First, 100 mg g- $\text{C}_3\text{N}_4$  was dispersed in 60 mL absolute ethanol and then sonicated by an ultrasonic cell disruptor for 30 min to obtain a uniformly dispersed g- $\text{C}_3\text{N}_4$  suspension. Second, 1 mg of synthesized porphyrin MOF was added into the above suspension under continuous sonication for another 10 min. Subsequently, the uniformly mixed suspension of the two materials was transferred to a 100 mL round-bottom flask and heated to reflux at 60 °C under stirring overnight. Finally, the as-prepared samples were collected by centrifugation and then evacuated at 160 °C for 12 h to remove any possible organic contaminants.

### 2.3. Characterization

The scanning electron microscopy (SEM) images were taken on a HITACHI SU-8010 microscope. Atomic force microscope (AFM) research was performed on a Bruker Dimension Icon MultiMode 8-HR with mica plate as the flat substrate with roughness of 0.1 nm. X-ray photoelectron spectroscopy (XPS) was conducted on a PHI Quantera SXM X-ray photoelectron spectrometer equipped with an Al X-ray excitation source (1486.6 eV). The binding energies (BE) were corrected by the C1s peak at 284.8 eV. Powder X-ray diffraction (PXRD) patterns of the samples were recorded on a Bruker D8-advance X-ray powder diffractometer operated at 40 kV voltage and 40 mA current with  $\text{CuK}\alpha$  radiation ( $\lambda = 1.5406 \text{ \AA}$ ). UV-vis diffuse reflectance spectrum (DRS) was obtained in a UV-vis spectrophotometer (UV-3900, HITACHI) using barium sulfate tablet as the absorb standard. Photoluminescence spectra (PL) were detected with a Hitachi F4600 fluorescence spectrophotometer. Fourier-transformed infrared spectra (FT-IR) were collected on a Bruker Vertex 70 V spectrometer equipped with a narrow band HgCdTe detector. Electron paramagnetic resonance (EPR) spectra were obtained with a Bruker Elexsys E500-T spectrometer with a liquid nitrogen cryostat at room temperature and 90 K. EPR acquisition parameters are: microwave frequency 9.44 GHz, microwave power 1 mW (23 dB), modulation amplitude 4 gauss, conversion time 40.96 ms, time constant 40.96 ms.

The EXAFS spectra were measured at 1W1B beamline in Beijing Synchrotron Radiation Facility (BSRF). The acquired EXAFS data were calculated and processed on the Athena program. During the experiment, copper foil,  $\text{Cu}_2\text{O}$  and CuO were used as references. All data were collected in fluorescence mode.

### 2.4. Electrochemical and photoelectrochemical tests

The photoelectrode was prepared according to the following typical

procedure: 5 mg of the sample (Cu-CuTCPP or g- $\text{C}_3\text{N}_4$ ) was added into a mixture of Nafion (10  $\mu\text{L}$ ) and ethanol (1 mL). Then, the obtained suspension (80  $\mu\text{L}$ ) was dropped onto the surface of an FTO plate with an area of  $2 \times 2 \text{ cm}$ . All measurements were performed on a workstation (CHI760E) in a standard three-electrode system configuration with the photocatalyst-coated FTO as the working electrode, Pt net as the counter electrode, and Ag/AgCl as the reference electrode. The flat-band potential of Cu-CuTCPP and g- $\text{C}_3\text{N}_4$  was determined by a standard Mott-Schottky method [39]. The measurements for the Mott-Schottky plots of samples were performed on an electrochemical workstation (Autolab, PGSTAT 302 N, Metrohm) in a standard three-electrode system configuration with the photocatalyst-coated FTO as the working electrode, Pt wire as the counter electrode, and Ag/AgCl as the reference electrode, 0.5 M  $\text{Na}_2\text{SO}_4$  solution as the electrolyte at frequencies of 500, 750, and 1000 Hz, respectively. Since it is generally accepted that the flat-band potential (quasi-Fermi level) in many n-type semiconductors is approximate 0.1 V lower than the conduction band minimum, combined with the DRS data that revealed the band gap ( $E_g$ ) of the semiconductor, the potentials of both conduction and valence band position can be calculated. The photocurrents and electrochemical impedance spectroscopy (EIS) measurements were performed in a conventional three electrode, single-compartment quartz cell on an electrochemical station (CHI 760D).  $\text{Na}_2\text{SO}_4$  solution (15 mL, 0.5 M) was used as the electrolyte and purged by  $\text{CO}_2$  flow for 30 min before irradiation. Transient photocurrent curves were recorded under chopped illuminations (20 s for each optical switch, light source: 360 nm ~ 800 nm, 100 mW/cm<sup>2</sup>) with no bias voltage [40]. The EIS tests were carried out under continuous light irradiation (360 nm ~ 800 nm, 100 mW/cm<sup>2</sup>) at 0.5 V and recorded over a frequency ranged from 0.01 to  $1 \times 10^5 \text{ Hz}$  with an AC voltage of 5 mV [41].

### 2.5. Activity tests of photocatalytic $\text{CO}_2$ reduction

The activity test was carried out in a homemade photochemical reactor. In a typical process, 5 mg photocatalyst was uniformly dispersed on a round quartz plate, while the sacrificial agents (mixture of 400  $\mu\text{L}$  water and 200  $\mu\text{L}$  TEA) were poured into a small cylindrical vessel and evaporated to react with the photocatalyst during the photoreactions. Then the photocatalysts loaded on the plate and vessel with sacrificial agents were placed in a 100 mL photochemical reactor with a quartz window on the top. The reactor was sealed and purged with pure  $\text{CO}_2$  for at least 20 min until no trace of  $\text{O}_2$  or  $\text{N}_2$  can be detected, and the pressure of the reactor was kept at 0.1 MPa. A 300 W Xenon lamp (Beijing Perfectlight, Microsolar 300) with both UV-cut and IR-cut filter (wavelength: 360–800 nm, 150 mW·cm<sup>-2</sup>) was used as the light source. The temperature of the reactor remained constant at 20 °C by cooling water circulation.

The gaseous product was monitored by gas chromatography (Fuli GC-2060) with a sampling (0.5 mL) interval of 1 h. The hydrocarbon products were analyzed by GC (Fuli GC-2060) with a flame ionization detector (FID) equipped with a 5  $\text{\AA}$  molecular column, while a thermal conductive detector (TCD) with a packed column (TDX-01) for  $\text{O}_2$  and  $\text{H}_2$ . CO was converted to  $\text{CH}_4$  by a methanation reactor prior to detection by another flame ionization detector.

<sup>13</sup>C<sub>2</sub>O<sub>2</sub> isotope labeling experiments were conducted under the same conditions, an Agilent 8890B gas chromatograph (GC) combined with a 5977B mass spectrometer (MS) was used to analyze the products of the isotopic experiments. The column used in GC-MS was HP-MOLESIEVE (30 m  $\times$  0.32 mm, Agilent Technologies, Serial number: USD 130113 H). The temperature of the inlet and oven was 150 and 35 °C, respectively. The carrier gas was helium (He) with a flow rate of 1.5 mL·min<sup>-1</sup>.



### 3. Results and discussion

#### 3.1. Structure characterization of the photocatalyst

The synthesis of 2D-MOF of Cu-CuTCPP was an adaption from the literature [42]: a bottom-up method was employed by reacting TCPP with  $\text{Cu}(\text{NO}_3)_2$ , while benzoic acid was added to be axially bound to the central Cu in porphyrin ring for a promoted anisotropic growth of the 2D MOF sheets. The UV-vis and FT-IR spectra (Fig. S2, SI) confirmed the metalation of porphyrin and the formation of MOF structure that was accordant with previous reports [42,43]. The ultrathin nanosheet morphology of the as-prepared Cu-CuTCPP was consolidated by the SEM images (Fig. 1a): the resultant sample appeared as a graphene-like thin layer and displayed a well-defined ultrathin 2D structure with the lateral size around 5  $\mu\text{m}$ . The thickness of the as-prepared Cu-CuTCPP was calibrated by AFM to be about 1 – 2 nm (Fig. 1e, f), which is close to graphene thickness.

For a better hybridization of 2D/2D structure between the two highly conjunctive components of g- $\text{C}_3\text{N}_4$  and Cu-CuTCPP, the as-synthesized g- $\text{C}_3\text{N}_4$  (Fig. 1b) was further exfoliated by an ultrasonic cell disruptor. Then the exfoliated g- $\text{C}_3\text{N}_4$  and Cu-CuTCPP samples were uniformly dispersed in ethanol with a feeding ratio of 100:1 (w/w) and heated to reflux at 60  $^\circ\text{C}$  to strengthen the interaction between the two components until the uniformly light-red-colored solid sample was obtained. The SEM images of the as-prepared samples showed that Cu-CuTCPP maintained the lamellar structure after attaching to g- $\text{C}_3\text{N}_4$  (Fig. 1c). The UV-vis diffuse reflectance spectrum (DRS) in Fig. S4 showed that compared with g- $\text{C}_3\text{N}_4$ , the absorption edge of the hybrid structure was notably red-shifted, in the meanwhile, the absorption maximum of the characteristic Q-band of Cu-CuTCPP at 539 nm was shifted to 548 nm, indicating the successful construction of  $\pi$ - $\pi$  stacking between g- $\text{C}_3\text{N}_4$  and Cu-CuTCPP MOF [44].

#### 3.2. Evaluation of the photocatalytic $\text{CO}_2$ reduction activity

Then the gas-solid photocatalytic  $\text{CO}_2$  reduction was conducted on the hybrid photocatalyst of Cu-CuTCPP/g- $\text{C}_3\text{N}_4$  with triethylamine (TEA) vapor as hole-scavenger, while the activities on individual components of either Cu-CuTCPP MOF or g- $\text{C}_3\text{N}_4$  were compared. As shown in Fig. 2a, on sole g- $\text{C}_3\text{N}_4$ , only a small amount of CO ( $1.7 \mu\text{mol}\cdot\text{g}^{-1}\cdot\text{h}^{-1}$ ) was detected, since the delocalized electron distributions in the metal-free  $\pi$ -conjugated structure of g- $\text{C}_3\text{N}_4$  are not in favor of  $\text{CO}_2$  trapping and activation. On the other hand, the Cu-CuTCPP alone also exhibited poor photocatalytic  $\text{CO}_2$  reduction activities with the almost undetectable evolution of CO. No further reduced products like  $\text{CH}_4$  or  $\text{C}_2\text{H}_6$  hydrocarbons were obtained on both individual components. In sharp contrast, on the hybrid photocatalyst, the generation of CO ( $12.3 \mu\text{mol}\cdot\text{g}^{-1}\cdot\text{h}^{-1}$ ) was seven times of that on g- $\text{C}_3\text{N}_4$ . More importantly,  $\text{CH}_4$  and  $\text{C}_2\text{H}_6$  were also produced in significant amounts of 11.6 and  $18.5 \mu\text{mol}\cdot\text{g}^{-1}\cdot\text{h}^{-1}$ , respectively. The generation of CO,  $\text{CH}_4$ , and  $\text{C}_2\text{H}_6$  all increased almost linearly with irradiation time (Fig. 2b) and the corresponding GC spectrum of peak sequence of  $\text{CH}_4$ ,  $\text{C}_2\text{H}_6$ , and CO was shown in Fig. S7a, b and c (SI). Among the  $\text{CO}_2$  reduction products, the selectivity of  $\text{C}_2\text{H}_6$  was as high as 44%, and when counting the total hydrocarbons ( $\text{CH}_4$  and  $\text{C}_2\text{H}_6$ ), the number was around 71%, to the best of our knowledge, such selectivity is hardly achieved in a photocatalytic system, either an inorganic-semiconductor-based one or MOF system (Table S1, SI) [45].  $\text{H}_2$  was not detected in our gas-solid reaction system, which would be originated from the advantage in the reagent concentration of gaseous  $\text{CO}_2$  compared to water vapor in the gas-solid reaction that remarkably suppressed the  $\text{H}_2$  production.

In addition, Cu-CuTCPP/g- $\text{C}_3\text{N}_4$  showed excellent performance stability in the cycle test: no notable decay of the activity was monitored during the five cycles (Fig. S5a, SI). Also, the XRD patterns, DRS spectra and SEM image (Fig. S6, SI) collected before and after reaction consolidated that the main structure of the hybrid catalyst kept stable during

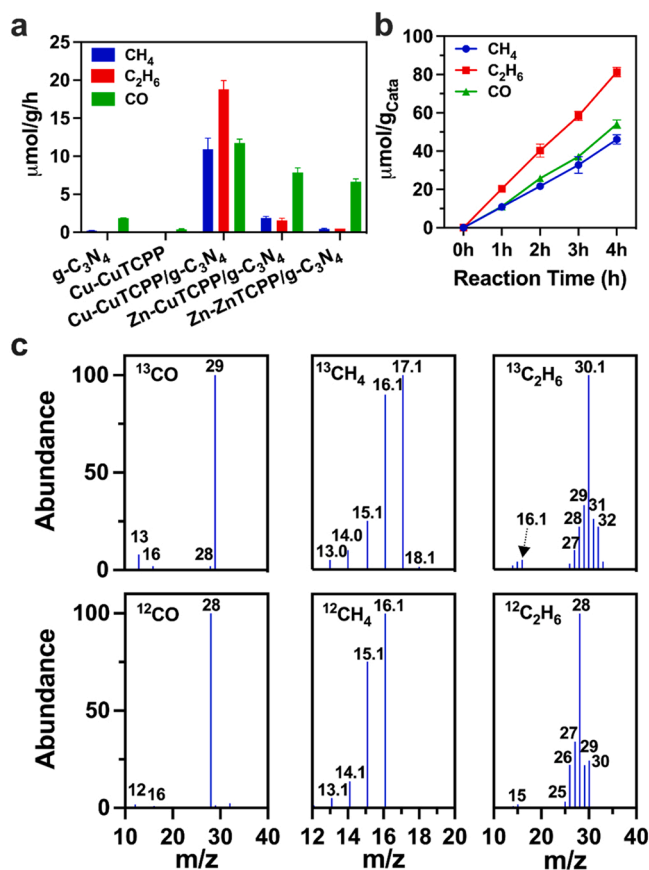


Fig. 2. a) Performance of photocatalytic  $\text{CO}_2$  reduction on g- $\text{C}_3\text{N}_4$ , Cu-CuTCPP, Cu-CuTCPP/g- $\text{C}_3\text{N}_4$ , Zn-CuTCPP/g- $\text{C}_3\text{N}_4$ , and Zn-ZnTCPP/g- $\text{C}_3\text{N}_4$ . b) Time course of photocatalytic  $\text{CO}_2$  reduction on Cu-CuTCPP/g- $\text{C}_3\text{N}_4$ . c) Mass spectra extracted from GC-MS analysis of CO,  $\text{CH}_4$ , and  $\text{C}_2\text{H}_6$  products in the presence of  $^{13}\text{CO}_2$  (top) or  $^{12}\text{CO}_2$  (bottom).

the whole reaction processes. When the experiment was conducted without photocatalyst or light, no detectable product was formed in the reaction system (Fig. S5b, SI). In order to further verify the source of the CO,  $\text{CH}_4$ , and  $\text{C}_2\text{H}_6$  products, an isotope experiment with  $^{13}\text{CO}_2$  instead of  $^{12}\text{CO}_2$  was carried out under identical photocatalytic reaction conditions, and the products were analyzed by gas chromatography and mass spectrometry. The GC-MS peak sequences of CO,  $\text{CH}_4$ ,  $\text{CO}_2$ , and  $\text{C}_2\text{H}_6$  are shown in Fig. S7d (SI), and the ion fragment analysis results of each peak are displayed in Fig. 2c, the molecular ion peak and all the fragment peaks of CO,  $\text{CH}_4$ , and  $\text{C}_2\text{H}_6$  shifted to their  $^{13}\text{C}$ -counterparts in the presence of  $^{13}\text{CO}_2$ . Therefore, it can be concluded that the generation of CO,  $\text{CH}_4$ , and  $\text{C}_2\text{H}_6$  is definitely derived from  $\text{CO}_2$  rather than other carbon sources.

#### 3.3. Identification of electron transfer direction in the hybrid structure

To explore the origin of the significantly promoted  $\text{CO}_2$  reduction activities and specific generation of C-C coupling hydrocarbons, the electron transfer between the two moieties of the hybrid photocatalyst was first investigated. The flat-band position of both individual components was calculated by electrochemical Mott-Schottky plots. The Mott-Schottky plots of g- $\text{C}_3\text{N}_4$  and Cu-CuTCPP were shown in Fig. S8b and d, respectively. The positive value of the slope ( $\text{C}^{-2}$  vs V) demonstrated the n-type semiconductor for both g- $\text{C}_3\text{N}_4$  and Cu-CuTCPP, [46] and the flat band potential for the two individual semiconductors can be determined to be  $-1.40$  and  $-1.20$  V (vs Ag/AgCl), respectively. It has been generally accepted that for n-type semiconductors, the flat-band potential (quasi-Fermi level) is located just 0.1 V below the

conduction band minimum (or LUMO), [39] therefore, the conduction band of g-C<sub>3</sub>N<sub>4</sub> and Cu-CuTCPP can be then counted to be  $-1.30$  V and  $-1.10$  V (vs NHE), respectively. Based on the bandgap of g-C<sub>3</sub>N<sub>4</sub> (2.80 eV) and Cu-CuTCPP (2.75 eV) estimated from the Tauc plot (Fig. S8a and c, SI), their valence band (or HOMO) potential can be then calculated to be 1.50 and 1.65 V vs NHE, respectively.

Accounting for the estimated band potentials, the hybrid Cu-CuTCPP/g-C<sub>3</sub>N<sub>4</sub> would be potentially a type-II heterojunction, in which the photogenerated electrons in g-C<sub>3</sub>N<sub>4</sub> transfer to the LUMO of Cu-CuTCPP. To consolidate such electron transfer, transient photoluminescence (PL) spectroscopy (Fig. 3a) as a useful tool for studying the behavior of electron-hole pairs in excited photocatalysts was employed. Since PL emission is caused by the recombination of electrons and holes, lower PL intensity generally indicates higher separation efficiency of electron-hole pairs [47]. With  $\pi$ - $\pi$  stacking between Cu-CuTCPP MOF and g-C<sub>3</sub>N<sub>4</sub>, the PL intensities of the hybrid photocatalyst declined to half in comparison with sole g-C<sub>3</sub>N<sub>4</sub>, moreover, the center of the PL band was redshifted from 445 to 455 nm. Meanwhile, the steady-state fluorescence (SSF) spectra showed that the average exciton lifetime decreased from 4.3 ns for g-C<sub>3</sub>N<sub>4</sub> to 3.2 ns for Cu-CuTCPP/g-C<sub>3</sub>N<sub>4</sub> heterojunctions. Also, in the transient photocurrent test in Fig. 3b, the photocurrent intensity on Cu-CuTCPP/g-C<sub>3</sub>N<sub>4</sub> was about three times of that on pristine g-C<sub>3</sub>N<sub>4</sub> when the light is on, which demonstrates its faster electron transfer rate [40]. In the electrochemical impedance spectroscopy (EIS) (Fig. 3c), the hybrid Cu-CuTCPP/g-C<sub>3</sub>N<sub>4</sub> exhibits a smaller radius than g-C<sub>3</sub>N<sub>4</sub>, indicative of a lower charge-transfer resistance [41]. All this data together identifies the much better charge-separation on Cu-CuTCPP/g-C<sub>3</sub>N<sub>4</sub> than the sole g-C<sub>3</sub>N<sub>4</sub> owing to the formation a heterojunction. Therefore, a much better charge-separation is identified on Cu-CuTCPP/g-C<sub>3</sub>N<sub>4</sub> than the sole g-C<sub>3</sub>N<sub>4</sub>.

Meanwhile, X-ray photoelectron spectroscopy (XPS) has been adopted to directly elucidate the electronic interaction between two components of a hybrid catalyst based on the shift of XPS peak position before and after the integration of two individual parts.<sup>38</sup> Herein, as shown in Fig. 4 (adapted from the full XPS spectra of g-C<sub>3</sub>N<sub>4</sub>, Cu-CuTCPP, and Cu-CuTCPP/g-C<sub>3</sub>N<sub>4</sub> in Fig. S9, SI), after the integration

of Cu-CuTCPP on g-C<sub>3</sub>N<sub>4</sub>, the C 1 s and N 1 s peaks of g-C<sub>3</sub>N<sub>4</sub> and the O 1 s of Cu-CuTCPP shifted to higher binding energies, whereas the Cu 2p peaks of Cu-CuTCPP shifted oppositely. This should indicate the electron extraction from g-C<sub>3</sub>N<sub>4</sub> to Cu-CuTCPP in the hybrid structure.

Moreover, to directly monitor the behaviors of the photogenerated electrons during the photocatalytic CO<sub>2</sub> reduction on g-C<sub>3</sub>N<sub>4</sub> or the hybrid Cu-CuTCPP/g-C<sub>3</sub>N<sub>4</sub> composites, a series of time-dependent attenuated-total-reflection infrared spectra (ATR-IR) upon illuminations were collected. Owing to the strong IR absorption of CN skeletal vibration, we mainly showed the IR region of 3600–1600 cm<sup>-1</sup>, and as exhibited in the top part of Fig. 3d, upon illumination in the presence of TEA and CO<sub>2</sub>, a monotonous baseline rising from 3600 cm<sup>-1</sup> to shorter wavenumbers was observed, which became more prominent with the extension of illumination time. This featureless baseline shifting was characteristic for the accumulated conduction band electrons in semiconductors, [48] and in this case, its occurrence can be explained as that when the photogenerated holes were scavenged by TEA, owing to the inefficient utilization of electrons through CO<sub>2</sub> reduction on g-C<sub>3</sub>N<sub>4</sub> as proved in the activity test (Fig. 2a), the electrons were left and accumulated in g-C<sub>3</sub>N<sub>4</sub>. In sharp contrast, on the hybrid Cu-CuTCPP/g-C<sub>3</sub>N<sub>4</sub>, the vast majority of the accumulated electrons were depleted as the intensity of baseline shifting was only around 1/7 of that on g-C<sub>3</sub>N<sub>4</sub> (Fig. 3d, bottom part). Therefore, g-C<sub>3</sub>N<sub>4</sub> and Cu-CuTCPP MOF form a type II heterojunction, during the CO<sub>2</sub> reduction, the electron generated in g-C<sub>3</sub>N<sub>4</sub> transferred to MOF and the CO<sub>2</sub> reduction was mainly conducted on Cu-CuTCPP MOF, [49,50] while the CO<sub>2</sub> reduction is mainly conducted on the surface of Cu-CuTCPP. Such efficient electron transfer in the  $\pi$ - $\pi$  stacking hybrid structure should be the premise for the generation of multielectron reduced products (C<sub>2</sub>H<sub>6</sub> and CH<sub>4</sub>).

### 3.4. Validation of the reconstruction of Cu-CuTCPP MOF

According to the analysis of the charge-separation process in the hybrid photocatalyst, we are now mainly shedding light on the behaviors of the Cu-CuTCPP moiety during the photocatalytic reaction to explore the origin of the C-C coupling products generation. On Cu-CuTCPP, two types of Cu sites exist, including the Cu<sub>N</sub> single site in

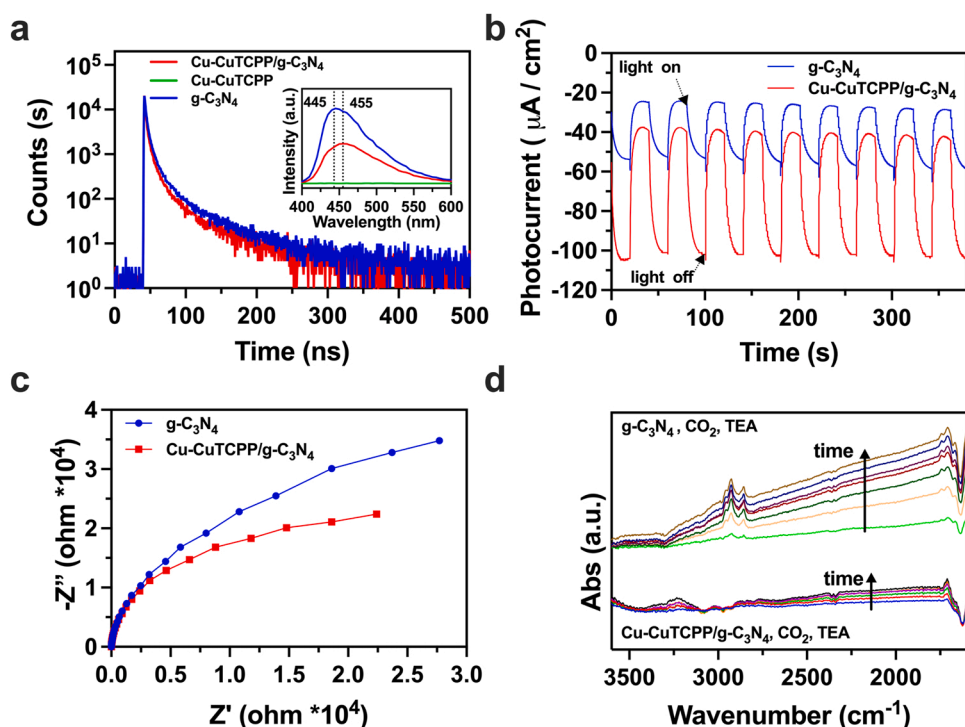


**Fig. 3.** a) Transient photoluminescence spectra (inset) of g-C<sub>3</sub>N<sub>4</sub>, Cu-CuTCPP, and Cu-CuTCPP/g-C<sub>3</sub>N<sub>4</sub> and fluorescence lifetime of g-C<sub>3</sub>N<sub>4</sub> and Cu-CuTCPP/g-C<sub>3</sub>N<sub>4</sub>. b) Photocurrent responses curves of g-C<sub>3</sub>N<sub>4</sub> and Cu-CuTCPP/g-C<sub>3</sub>N<sub>4</sub> in 0.5 M Na<sub>2</sub>SO<sub>4</sub> solution saturated by CO<sub>2</sub> as the electrolyte. c) Electrochemical impedance spectroscopy of g-C<sub>3</sub>N<sub>4</sub> and Cu-CuTCPP/g-C<sub>3</sub>N<sub>4</sub>. d) Time-dependent in-situ ATR-IR spectra of g-C<sub>3</sub>N<sub>4</sub> and Cu-CuTCPP/g-C<sub>3</sub>N<sub>4</sub> upon illuminations in the presence of CO<sub>2</sub> and TEA.

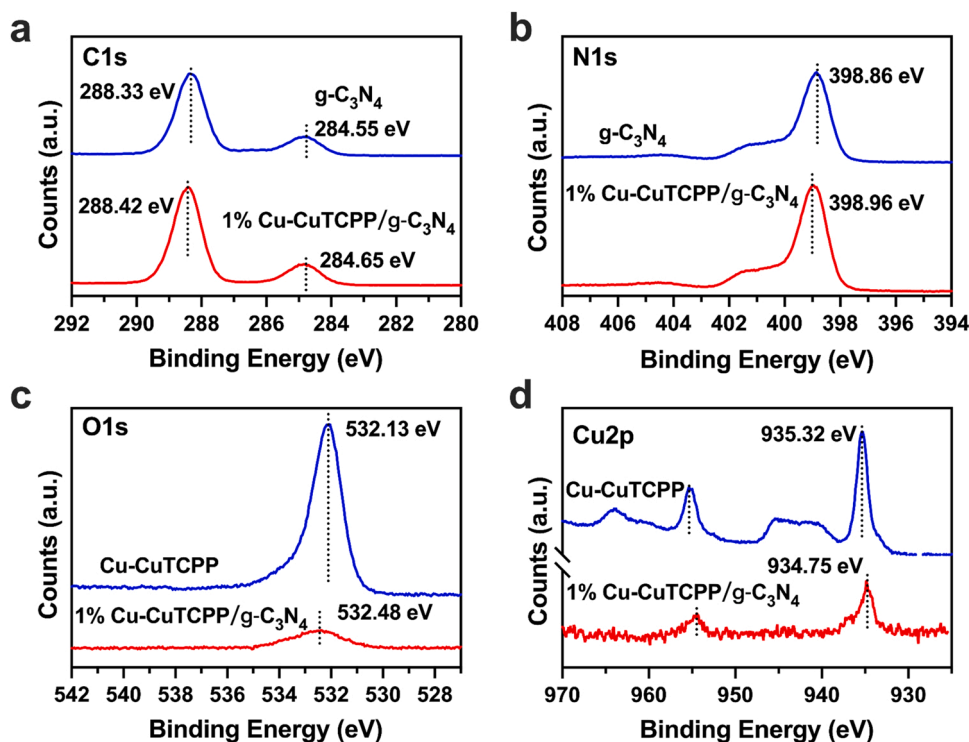


Fig. 4. XPS spectra of g-C<sub>3</sub>N<sub>4</sub>, Cu-CuTCPP, and Cu-CuTCPP/g-C<sub>3</sub>N<sub>4</sub>.

the center of the porphyrin ring and the paddle-wheel Cu<sub>2</sub>(COO)<sub>4</sub> nodes [42]. To identify the roles of these two sites in CO<sub>2</sub> reduction, Zn-CuTCPP/g-C<sub>3</sub>N<sub>4</sub> and Zn-ZnTCPP/g-C<sub>3</sub>N<sub>4</sub>, which used Zn to replace Cu<sub>2</sub>(COO)<sub>4</sub> sites or both Cu sites, were synthesized via a similar procedure and the photocatalytic CO<sub>2</sub> reduction was also conducted on both samples. The synthesis of Cu-ZnTCPP was not achieved, it seems that Cu<sup>2+</sup> coordinates with TCPP more strongly than Zn<sup>2+</sup>, then the synthetic approach started from ZnTCPP and Cu(NO<sub>3</sub>)<sub>2</sub> finally resulted in the formation of Cu-CuTCPP rather than Cu-ZnTCPP. The replacement of Cu<sup>II</sup> by Zn<sup>II</sup> is on account of the close electronic structure (with one more 3d electron) but divergent CO<sub>2</sub> reaction activities between these two metal sites: whereas Zn-based catalyst is not regarded to be efficient in CO<sub>2</sub> reduction and no production of C<sub>2</sub><sup>+</sup> hydrocarbons has been reported. As shown in Fig. 2a, for Zn-CuTCPP/g-C<sub>3</sub>N<sub>4</sub> that substituting Cu<sub>2</sub>(COO)<sub>4</sub> to Zn<sub>2</sub>(COO)<sub>4</sub>, the generation of C<sub>2</sub>H<sub>6</sub> (1.5 μmol·g<sup>-1</sup>·h<sup>-1</sup>) was significantly suppressed by 92% of that on Cu-CuTCPP/g-C<sub>3</sub>N<sub>4</sub>, together with the 83% decrease in CH<sub>4</sub> production (2.0 μmol·g<sup>-1</sup>·h<sup>-1</sup>). The generation of CO also decreased about 1/3 (7.3 μmol·g<sup>-1</sup>·h<sup>-1</sup>). When further replacing CuN<sub>4</sub> to ZnN<sub>4</sub>, although the CO generation only slightly declined, the production of hydrocarbons drastically decreased to a trace amount. Therefore, it can be concluded that on Cu-CuTCPP, it is the Cu<sub>2</sub>(COO)<sub>4</sub> node rather than the CuN<sub>4</sub> site that mainly being responsible for the CO<sub>2</sub> reduction to CH<sub>4</sub> and the C-C coupling products of C<sub>2</sub>H<sub>6</sub>.

To explore the detailed mechanism of CO<sub>2</sub> reduction to CH<sub>4</sub> and C<sub>2</sub>H<sub>6</sub> on Cu<sub>2</sub>(COO)<sub>4</sub> node, a structural analysis of Cu<sub>2</sub>(COO)<sub>4</sub> node before and after the photocatalytic reactions, including the coordination circumstances and valence states of Cu, was conducted by electronic paramagnetic resonance (EPR) spectroscopy together with X-ray absorption fine structure (XAFS) spectroscopy.

In EPR studies, the solid powder of cupric acetate containing a typical Cu<sup>II</sup><sub>2</sub>(COO)<sub>4</sub> paddle-wheel structure was first investigated as a standard. Both monomer (Cu<sup>II</sup>Ac<sub>2</sub>) and dimer (Cu<sup>II</sup><sub>2</sub>Ac<sub>4</sub>) exist in cupric acetate samples, leading to the occurrence of three types of electronic states with two of them EPR-active. For a dimer Cu<sup>II</sup><sub>2</sub>(COO)<sub>4</sub> paddle-wheel structure with two 3d<sup>9</sup> Cu<sup>II</sup>, the magnetic coupling between the

two Cu<sup>II</sup> ions leads to the existence of two thermally interconvertible states: the antiferromagnetically coupled singlet (*S*=0) and ferromagnetically coupled triplet (*S*=1) (with the triplet ~300 cm<sup>-1</sup> above the singlet state) [51]. As shown in Fig. 5a, both at 90 K and room temperature, the EPR signal for Δ*m<sub>s</sub>* = ± 2 and Δ*m<sub>s</sub>* = ± 1 in triplet Cu<sup>II</sup><sub>2</sub>(COO)<sub>4</sub> can be observed, while another signal at *g* = 2.19 can be assigned to the doublet state (*S*=1/2) of monomer Cu<sup>II</sup>(COO)<sub>2</sub>.

In the EPR spectrum of Cu-CuTCPP MOF collected at 90 K (Fig. 5b, black curve), only the signal for the doublet (*S*=1/2) Cu<sup>II</sup>N<sub>4</sub> (principal *g* values around *g<sub>xx</sub>* = *g<sub>yy</sub>* = 2.05, *g<sub>zz</sub>* = 2.19) was observed, with the *g* values and overall envelop consistent with previously reported spectra of copper porphyrins [52]. The absence of the signal for the triplet paddle-wheel Cu<sup>II</sup><sub>2</sub>(COO)<sub>4</sub> as in Fig. 5a suggests that Cu-node in the 2D-MOF is in its singlet ground state at low temperature. When the system warmed up to room temperature (Fig. 5b, red curve), a new set of signals appeared at < 1000 G and the 4400–5000 G region, which should be assigned to the Δ*m<sub>s</sub>* = ± 2 and Δ*m<sub>s</sub>* = ± 1 signals of the thermally accessible triplet excited state of Cu<sup>II</sup><sub>2</sub>(COO)<sub>4</sub> [53,54]. The lack of visible triplet signal at 90 K implies wider singlet-triplet (*S*-*T*) separation energy, i.e. 2 *J* > 300 cm<sup>-1</sup>. Since the *S*-*T* separation of such bimetallic site is sensitive to the types and geometries of the bridging ligands, as well as the direct overlap of metal *d* orbitals [55]. The different peak shapes from the cupric acetate dimers imply that compared with the free one in Cu<sub>2</sub>(Ac)<sub>4</sub>, the incorporation of the paddle-wheel structure into the MOF network altered Cu-Cu distances as well as Cu-(RCO<sub>2</sub>)-Cu bond angles, resulting in a geometry more favorable to antiferromagnetic coupling.

When the Cu-CuTCPP MOF was incorporated with g-C<sub>3</sub>N<sub>4</sub> to form the hybrid structure, the EPR spectrum collected at 90 K exhibited a main feature around *g* = 2.1 consistent with a Cu<sup>II</sup>-porphyrin (Cu<sup>II</sup>N<sub>4</sub>) species, as well as the tiny g-C<sub>3</sub>N<sub>4</sub> defect signal at *g* = 2.0 (Fig. 5c). Interestingly, neither a clear signal belonging to a thermally excited state at room temperature nor a ground state triplet signal at 90 K can be observed. This leads us to conclude that the dicupric paddle-wheel site in the integrated MOF/g-C<sub>3</sub>N<sub>4</sub> mainly stays in an EPR-silent singlet state both at 90 K and room temperature, with a triplet-singlet separation

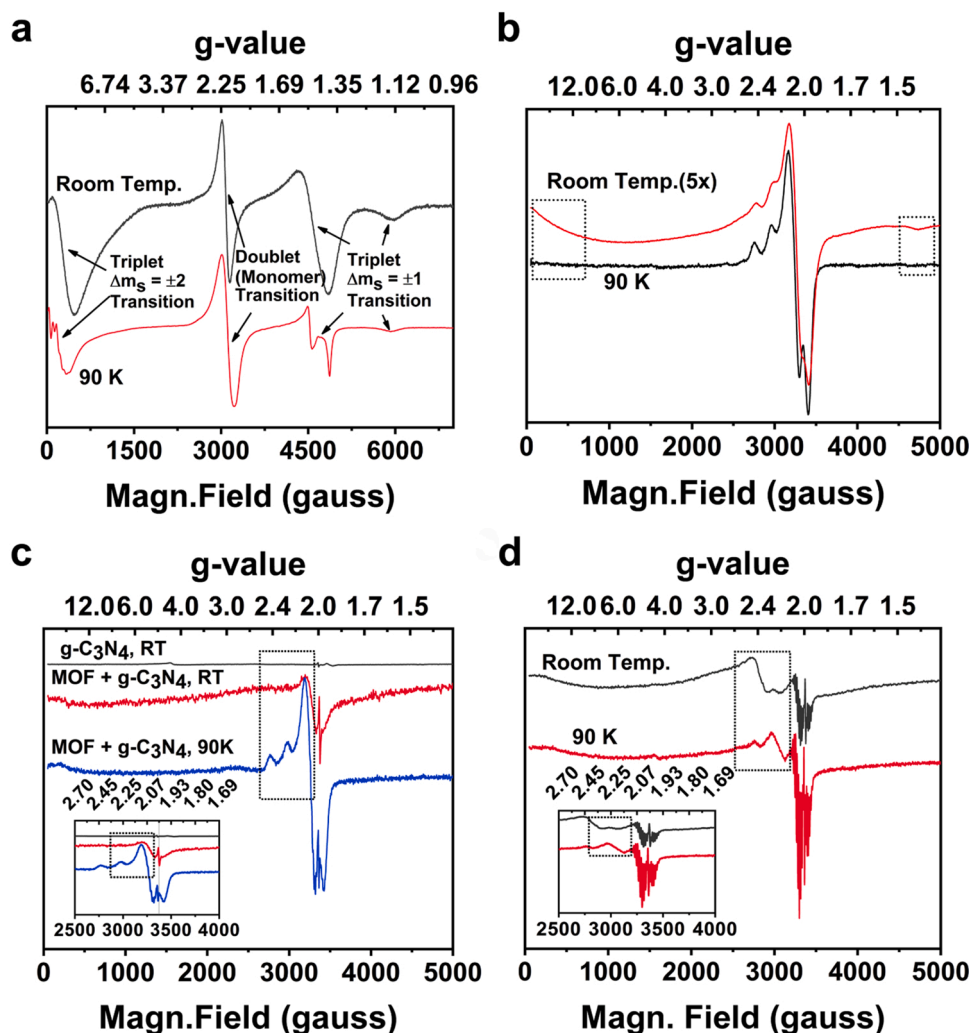


**Fig. 5.** EPR spectra of a) cupric acetate and b) Cu-CuTCPP at 90 K and room temperature (RT), c) g-C<sub>3</sub>N<sub>4</sub> (RT) and Cu-CuTCPP/g-C<sub>3</sub>N<sub>4</sub> (90 K and RT) before photocatalytic reactions. d) in situ EPR spectra of Cu-CuTCPP/g-C<sub>3</sub>N<sub>4</sub> (90 K and RT) after illumination for 1 h in the presence of TEA and CO<sub>2</sub>. The insets in c) and d) display the enlarged spectra between 2500 and 4000 Gs.

(2 J) becoming even greater than MOF-only case. It would be most possible that the interaction between g-C<sub>3</sub>N<sub>4</sub> and Cu-CuTCPP MOF affect the structure of Cu<sup>II</sup><sub>2</sub>(COO)<sub>4</sub>, i.e., shortening the distance between the two Cu<sup>II</sup> sites, then the enhanced *d-d* coupling increased the S-T barrier and caused the much smaller population of triplet state bands at room temperature to be clearly observed.

After the 1 h in-situ photocatalytic reaction in the presence of TEA and CO<sub>2</sub>, the EPR features of Cu-CuTCPP notably changed (Fig. 5d). For the signal of CuN<sub>4</sub>, the principal g values remained unchanged, indicating the stable coordination and valance state of Cu in CuN<sub>4</sub> before and after the photoreactions. On the other hand, the “superhyperfine” structure coming from <sup>63/65</sup>Cu and <sup>14</sup>N of the Cu<sup>II</sup>-porphyrin site becomes well-resolved (Fig. 5d inset) compared to the Cu-CuTCPP before reaction, which can indicate a decrease of the amount of surrounding paramagnetic sites, i.e., the reduction of paramagnetic Cu<sup>II</sup> in paddle-wheel Cu-node into diamagnetic Cu<sup>I</sup> as revealed in the following XANES results (Fig. 6a).

Simultaneously with this observed hyperfine-split CuN<sub>4</sub> signal, a very broad (~200 gauss) signal around g = 2.25 appeared at room temperature and becomes prominent at 90 K (Fig. 5d inset). Although the paddle-wheel Cu<sup>II</sup>-node in its singlet state is EPR-silent as discussed above, once one of two Cu<sup>II</sup> is reduced to Cu<sup>I</sup> as the form of Cu<sup>II</sup>Cu<sup>I</sup>(-COO)<sub>3</sub> (one carboxylate disassociated to balance the charge), this mixed-valence dual-Cu site should be EPR-active exhibiting a g value

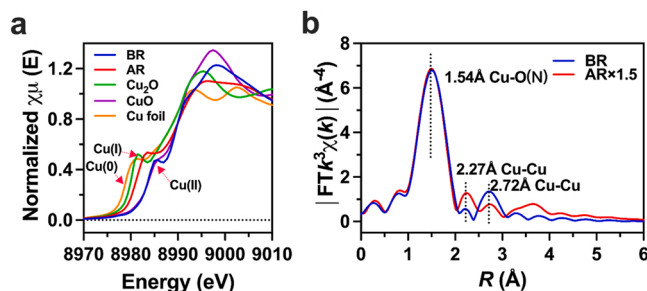


**Fig. 6.** a) Copper K-edge X-ray absorption near-edge structure (XANES) spectra on pristine Cu<sup>0</sup> foil, Cu<sub>2</sub>O, CuO, and Cu-CuTCPP/g-C<sub>3</sub>N<sub>4</sub> before (BR) and after (AR) 3 h-photocatalytic CO<sub>2</sub> reduction. b) Fourier transformed K<sup>3</sup>-weighted  $\chi(k)$  function of EXAFS for Cu-CuTCPP/g-C<sub>3</sub>N<sub>4</sub> before (BR) and after (AR) reaction.

close to the monomer Cu<sup>II</sup>(Ac)<sub>2</sub> at around 2.20 (Fig. 5a). Furthermore, when the single unpaired electron is delocalized between two Cu, and the structure is resonating between [Cu<sup>I</sup>A Cu<sup>II</sup>B] ↔ [Cu<sup>II</sup>A Cu<sup>I</sup>B], the EPR signal should exhibit as seven Cu hyperfine lines with about half of the splitting magnitude of a single Cu<sup>II</sup>, and an intensity ratio of 1:2:3:4:3:2:1, [56] but this hyperfine feature is often obscured by the



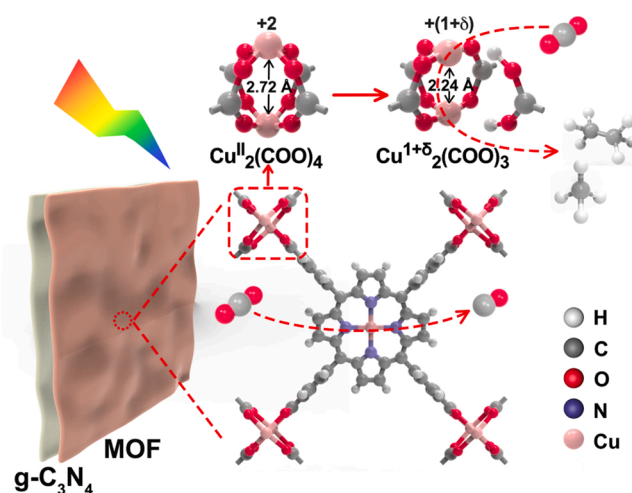
partial overlapping of broad lines, emerging as broad signals, losing all detailed information about individual sites [57]. Therefore, the  $g = 2.25$  signal should be assigned to the partly reduced  $\text{Cu}^{\text{II}}\text{Cu}^{\text{I}}(\text{COO})_3$  node formed during the reaction, and the broadening of the signal should indicate the electron redistribution between the two Cu as the form of  $\text{Cu}^{1+\delta}_2(\text{COO})_3$ .

The structural alternation of Cu-node during the photoreactions was also validated by XAFS studies. In Cu K-edge X-ray absorption near edge structure (XANES) of Cu-CuTCPP/g- $\text{C}_3\text{N}_4$  (Fig. 6a), for the sample before photocatalytic reactions (BR), the pre-edge of the spectrum was almost overlapped with that of the standard CuO, confirming the initial valence states of all the copper sites to be +2. As shown by the standard spectra of CuO,  $\text{Cu}_2\text{O}$ , and  $\text{Cu}^0$  foil, the shifting of the pre-edge position to lower energy would suggest a decrease in the valence state of Cu. After a 3 h reaction, the recollected sample (AR) exhibited a pre-edge between  $\text{Cu}^{\text{II}}$  and  $\text{Cu}^{\text{I}}$ , which demonstrates that partial of the  $\text{Cu}^{\text{II}}$  sites was reduced to  $\text{Cu}^{\text{I}}$  during the photocatalytic reactions. As a comparison, the Cu K-edge XANES of Zn-CuTCPP/g- $\text{C}_3\text{N}_4$  that contains only  $\text{CuN}_4$  sites (Fig. S10a, SI), and the Zn K-edge EXAFS of Zn-CuTCPP/g- $\text{C}_3\text{N}_4$  contains Zn node (Fig. S10b, SI) remained almost unchanged after photoreaction, therefore, we can clearly draw the conclusion that the partial reduction of  $\text{Cu}^{\text{II}}$  to  $\text{Cu}^{\text{I}}$  and reconstruction mainly occurred on the  $\text{Cu}_2(\text{COO})_4$  site.

The Cu K-edge extended X-ray absorption fine structure (EXAFS) of Cu-CuTCPP/g- $\text{C}_3\text{N}_4$  catalyst before and after photocatalysis were also collected to probe the inherent structure (Fig. 6b). For the hybrid catalyst before photoreaction, the Cu-O(N) peak around 1.54 Å and Cu-Cu peak around 2.72 Å (uncorrected for the photoelectron phase shift) were observed, after 3 h-photocatalytic  $\text{CO}_2$  reduction, a Cu-Cu peak at 2.27 Å similar to that in Cu foil appeared, accompanied by a drop in the intensity of 2.72 Å peak. EXAFS curve fitting further reveals that the coordination number of the nearest-neighbor O atoms surrounding the Cu atoms decreased from 3.8 before reaction to 3.0 after reaction (Fig. S11, Table S2, SI), which is very close to the theoretical O-coordination number change when one of the  $\text{Cu}^{\text{II}}$  in  $\text{Cu}^{\text{II}}_2(\text{COO})_4$  node is reduced to  $\text{Cu}^{\text{I}}$  ( $\text{Cu}^{\text{II}}\text{Cu}^{\text{I}}(\text{COO})_3$ ), as the dissociation of approximate 1/4 of Cu-O bonds in the node structure is the adaption for charge balance after partial reduction. The appearance of a 2.27 Å peak at the expense of the depletion of 2.72 Å peak should suggest the closer Cu-Cu distance after the  $\text{Cu}^{\text{II}}_2(\text{COO})_4$  node was partially reduced to  $\text{Cu}^{\text{II}}\text{Cu}^{\text{I}}(\text{COO})_3$ . Moreover, when considering that the radius of the Cu atom is approximately 1.28 Å, a partial electron density overlapping between the two Cu atoms in  $\text{Cu}^{\text{II}}\text{Cu}^{\text{I}}(\text{COO})_3$ , the reconstructed Cu-node, is expected. This electron density overlapping would induce an electron-redistribution between the two Cu in the node to exhibit as the form of  $\text{Cu}^{1+\delta}_2(\text{COO})_3$ , which was also indicated in EPR results.

Therefore, based on the combined XAFS and EPR results, reconstruction in the Cu-CuTCPP moiety of the hybrid catalyst during the photocatalytic reactions is uncovered, as shown in Scheme 1. In the reconstruction, the valence state of Cu in  $\text{CuN}_4$  site keeps almost unchanged, whereas the node site undergoes a partial reduction and dissociation of carboxylate ligand to form  $\text{Cu}^{1+\delta}_2(\text{COO})_3$  with a shortened Cu-Cu distance.

Based on the activity test in Fig. 2a, on Cu-CuTCPP/g- $\text{C}_3\text{N}_4$ , the two types of Cu sites,  $\text{CuN}_4$  single-site and Cu-node exhibit distinctive activities in  $\text{CO}_2$  reduction: the former mainly reduces  $\text{CO}_2$  to CO, while the latter achieves the deep reduction to  $\text{CH}_4$  and  $\text{C}_2\text{H}_6$ . For the  $\text{CO}_2$  reduction to  $\text{C}_2\text{H}_6$ , the reported mechanisms were varied [58,59]. Herein, as shown in Fig. 2a, the generation of  $\text{C}_2\text{H}_6$  is synchronized with that of  $\text{CH}_4$  on all of Cu-CuTCPP/g- $\text{C}_3\text{N}_4$ , Zn-CuTCPP/g- $\text{C}_3\text{N}_4$  and Zn-ZnTCPP/g- $\text{C}_3\text{N}_4$ , demonstrating the relationship between generation of these two products on our photocatalysts. Also considering the absence of  $\text{C}_2\text{H}_4$  generation, the most possible pathway for  $\text{C}_2\text{H}_6$  production would be the coupling of  $\text{CH}_4$  via  $\text{CO}_2 \rightarrow \text{CO} \rightarrow \text{CH}_4 \rightarrow \cdot\text{CH}_3 + \cdot\text{CH}_3 \rightarrow \text{C}_2\text{H}_6$ , [60] In general, the reduction of  $\text{CO}_2$  to hydrocarbons goes through CO, a key intermediate, and therefore CO should be the key intermediate for the formation of  $\text{CH}_4$  and  $\text{C}_2\text{H}_6$ . Then the trap of the in



**Scheme 1.** The self-reconstruction of paddle-wheel Cu-node during the photocatalytic  $\text{CO}_2$  reduction.

situ generated CO from  $\text{CO}_2$  reduction on the catalytic site is of particular significance, [27] especially the less efficient electron transfer in the photocatalytic system requires a longer residence time of CO on the catalytic sites to accept the subsequent electrons to be further reduced [61]. Therefore, the CO adsorption on Cu-node before and after the photocatalytic  $\text{CO}_2$  reduction was investigated. As shown in the IR spectra of CO adsorption (Fig. 7), for Cu-CuTCPP/g- $\text{C}_3\text{N}_4$  before photocatalytic reactions, no notable adsorbed CO band can be observed, whereas, when introducing CO to the sample after 3 h photoreactions, two major bands appeared. The first band at  $2118\text{ cm}^{-1}$  should be assigned to linearly adsorbed CO on newly formed  $\text{Cu}^{1+\delta}$  sites in the node, [62] while the other band at  $2005\text{ cm}^{-1}$  has the IR frequency lower than the reported numbers for linearly adsorbed CO either on  $\text{Cu}^{\text{I}}$  or  $\text{Cu}^0$  sites [63]. Since the two Cu sites in  $\text{Cu}^{1+\delta}_2(\text{COO})_3$  have a very close distance and an electron density redistribution between these two Cu is proposed, this  $2005\text{ cm}^{-1}$  band should be originated from the bridged CO adsorbed on these two adjacent Cu. Such IR spectra observation confirms a much stronger CO adsorption on the reconstructed Cu-node than the original one.

Another key feature of the reconstructed  $\text{Cu}^{1+\delta}_2(\text{COO})_3$  node that would lead to the facilitated generation of  $\text{C}_2\text{H}_6$  is the dissociation of 1/4 of carboxylate-coordination. It has been well accepted that the generation of C-C coupling products from  $\text{CO}_2$  requires the synergistic action of multiple reaction sites, thus, the Cu-node containing dual Cu sites in

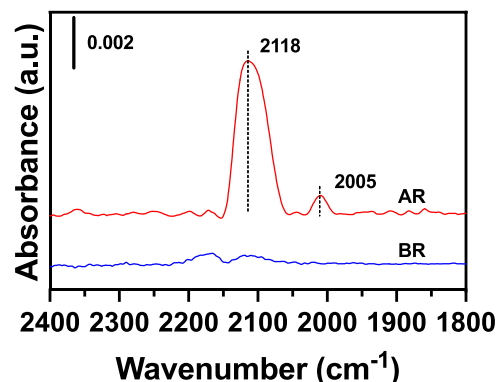


**Fig. 7.** IR spectra of CO adsorption on CuTCPP/g- $\text{C}_3\text{N}_4$  before and after 3 h photocatalytic  $\text{CO}_2$  reduction. For clarification, the P and R branches at  $2173$  and  $2120\text{ cm}^{-1}$  for gaseous CO were subtracted using the standard spectra collected from the sample-free chamber containing an identical concentration of gaseous CO.



neighboring distance would be potentially active for such C-C coupling reaction, however, the reaction of CO<sub>2</sub> from the open side (above the plane of 2D-MOF) of Cu-node cannot utilize both Cu sites in the node, especially when the Cu-node is coordination-saturated with four carboxylates in its original form of Cu<sup>II</sup>(COO)<sub>4</sub>. As shown in Scheme 1, the reconstruction to Cu<sup>I+δ</sup><sub>2</sub>(COO)<sub>3</sub> node remarkably lowers down the steric hindrance, benefiting the CO<sub>2</sub> reduction synergistically conducted on both Cu sites from the side of MOF pores for an enhanced possibility of C-C coupling. Moreover, the confinement effect of the MOF pore and paddle-wheel cage extends the stay of the intermediate products around the Cu catalytic site, [64] and the dissociated carboxylate can also play the role as proton relay to transfer protons to the Cu catalytic site to assist the formation of C-H bond [65]. Such coordinatively unsaturated Cu paddle-wheel structure has also been theoretically demonstrated to favor the formation of CH<sub>4</sub> and C-C coupling product in a very recent work [66].

#### 4. Conclusions

In conclusion, we successfully fabricated a  $\pi$ - $\pi$  stacking hybrid structure between two highly conjunctive materials of g-C<sub>3</sub>N<sub>4</sub> and 2D-MOF of Cu-CuTCPP, in which the former part acts as the photosensitizer to provide electrons, while the latter displays as the interface to catalyze CO<sub>2</sub> reduction. The hybrid catalyst exhibits the activities to photocatalytically convert CO<sub>2</sub> to C-C coupling products of C<sub>2</sub>H<sub>6</sub> in a high selectivity that is hardly achieved in a photocatalytic system. A light-driving reconstruction of Cu-CuTCPP moiety by the photo-generated electrons from excited g-C<sub>3</sub>N<sub>4</sub> is identified. Remaining the CuN<sub>4</sub> single-site unchanged, the self-reconstruction mainly alters the structure of the Cu<sub>2</sub>(COO)<sub>4</sub> node, which is the origin for the specific activity of C<sub>2</sub>H<sub>6</sub> generation. This work, for the first time, uncovers the detailed mechanism that how the node site of MOF is participating in the photocatalytic CO<sub>2</sub> reduction and provides a new strategy to achieve the reduction of CO<sub>2</sub> to C<sub>2+</sub> hydrocarbons in a photocatalytic system.

#### CRediT authorship contribution statement

**Shijie Xie:** Conceptualization, Methodology, Formal analysis, Investigation, Data curation, Writing – original draft, Visualization. **Yangfan Li:** Investigation, Methodology, Data curation. **Bo Sheng:** Methodology, Data curation. **Wanyi Zhang:** Methodology, Data curation. **Wei Wang:** Methodology, Data curation. **Jikun Li:** Writing – review & editing, Methodology. **Chuncheng Chen:** Writing – review & editing, Supervision. **Jincai Zhao:** Writing – review & editing, Supervision. **Hua Sheng:** Resources, Conceptualization, Writing – review & editing, Supervision, Project administration, Funding acquisition.

#### Declaration of Competing Interest

The authors declare that they have no known competing financial interests or personal relationships that could have appeared to influence the work reported in this paper.

#### Acknowledgements

This work was supported by the National Key Research and Development Program of China (No. 2020YFA0710303 and 2020YFC1808401), the National Natural Science Foundation of China (No. 22076193 and 21827809), and the “Strategic Priority Research Program B” of the Chinese Academy of Sciences (Grant No. XDB36000000). The authors thank the photoemission beamline 1W1B station of the Beijing Synchrotron Radiation Facility (BSRF) for XAFS measurements.

#### Appendix A. Supporting information

Supplementary data associated with this article can be found in the online version at doi:10.1016/j.apcatb.2022.121320.

#### References

- [1] G.A. Olah, G.K. Prakash, A. Goepfert, Anthropogenic chemical carbon cycle for a sustainable future, *J. Am. Chem. Soc.* 133 (2011) 12881–12898, <https://doi.org/10.1021/ja202642y>.
- [2] M. Aresta, A. Dibenedetto, A. Angelini, Catalysis for the valorization of exhaust carbon: from CO<sub>2</sub> to chemicals, materials, and fuels. technological use of CO<sub>2</sub>, *Chem. Rev.* 114 (2014) 1709–1742, <https://doi.org/10.1021/cr4002758>.
- [3] A.J. Morris, G.J. Meyer, E. Fujita, Molecular approaches to the photocatalytic reduction of carbon dioxide for solar fuels, *Acc. Chem. Res.* 42 (2009) 1983–1994, <https://doi.org/10.1021/ar9001679>.
- [4] S.S. Mao, S. Shen, Catalysing artificial photosynthesis, *Nat. Photonics* 7 (2013) 944–946, <https://doi.org/10.1038/nphoton.2013.326>.
- [5] X. Feng, Y. Pi, Y. Song, C. Brzezinski, Z. Xu, Z. Li, W. Lin, Metal-organic frameworks significantly enhance photocatalytic hydrogen evolution and CO<sub>2</sub> reduction with earth-abundant copper photosensitizers, *J. Am. Chem. Soc.* 142 (2020) 690–695, <https://doi.org/10.1021/jacs.9b12229>.
- [6] X.Y. Dao, X.F. Xie, J.H. Guo, X.Y. Zhang, Y.S. Kang, W.Y. Sun, Boosting photocatalytic CO<sub>2</sub> reduction efficiency by heterostructures of NH<sub>2</sub>-MIL-101(Fe)/g-C<sub>3</sub>N<sub>4</sub>, *ACS Appl. Energy Mater.* 3 (2020) 3946–3954, <https://doi.org/10.1021/acsaem.0c00352>.
- [7] A. Nakada, K. Koike, T. Nakashima, T. Morimoto, O. Ishitani, Photocatalytic CO<sub>2</sub> reduction to formic acid using a Ru(II)-Re(I) supramolecular complex in an aqueous solution, *Inorg. Chem.* 54 (2015) 1800–1807, <https://doi.org/10.1021/ic502707t>.
- [8] P. Li, L. Liu, W. An, H. Wang, H. Guo, Y. Liang, W. Cui, Ultrathin porous g-C<sub>3</sub>N<sub>4</sub> nanosheets modified with AuCu alloy nanoparticles and C-C coupling photothermal catalytic reduction of CO<sub>2</sub> to ethanol, *Appl. Catal. B Environ.* 266 (2020) 118618–118632, <https://doi.org/10.1016/j.apcatb.2020.118618>.
- [9] H. Li, J. Zhang, J. Yu, S. Cao, Ultra-thin carbon-doped Bi<sub>2</sub>WO<sub>6</sub> nanosheets for enhanced photocatalytic CO<sub>2</sub> reduction, *Trans. Tianjin Univ.* 27 (2021) 338–347, <https://doi.org/10.1007/s12209-021-00289-5>.
- [10] H.B. Zhang, J. Wei, J.C. Dong, G.G. Liu, L. Shi, P.F. An, G.X. Zhao, J.T. Kong, X. J. Wang, X.G. Meng, J. Zhang, J.H. Ye, Efficient visible-light-driven carbon dioxide reduction by a Single-Atom implanted metal-organic framework, *Angew. Chem. Int. Ed.* 55 (2016) 14310–14314, <https://doi.org/10.1002/anie.201608597>.
- [11] J.D. Yi, R. Xie, Z.L. Xie, G.L. Chai, T.F. Liu, R.P. Chen, Y.B. Huang, R. Cao, Highly selective CO<sub>2</sub> electroreduction to CH<sub>4</sub> by in situ generated Cu<sub>2</sub>O single-type sites on a conductive MOF: stabilizing key intermediates with hydrogen bonding, *Angew. Chem. Int. Ed.* 59 (2020) 23641–23648, <https://doi.org/10.1002/anie.202010601>.
- [12] X.J. Yang, T.F. Liu, M. Zhang, B. Song, Q.Y. Li, J.J. Yang, Interfacial dual vacancies modulating electronic structure to promote the separation of photogenerated carriers for efficient CO<sub>2</sub> photoreduction, *Appl. Surf. Sci.* 551 (2021) 149035–149043, <https://doi.org/10.1016/j.apsusc.2021.149035>.
- [13] Z.Y. Jiang, W.K. Miao, X.L. Zhu, G.H. Yang, Z.M. Yuan, J.C. Chen, X.X. Ji, F. G. Kong, B.B. Huang, Modifying lewis base on TiO<sub>2</sub> nanosheets for enhancing CO<sub>2</sub> adsorption and the separation of photogenerated charge carriers, *Appl. Catal. B Environ.* 256 (2019) 117881–117888, <https://doi.org/10.1016/j.apcatb.2019.117881>.
- [14] S. Wang, B.Y. Guan, X.W.D. Lou, Construction of ZnIn<sub>2</sub>S<sub>4</sub>-In<sub>2</sub>O<sub>3</sub> hierarchical tubular heterostructures for efficient CO<sub>2</sub> photoreduction, *J. Am. Chem. Soc.* 140 (2018) 5037–5040, <https://doi.org/10.1021/jacs.8b02200>.
- [15] D.C. Liu, T. Ouyang, R. Xiao, W.J. Liu, D.C. Zhong, Z. Xu, T.B. Lu, Anchoring Co(II) ions into a thiol-laced metal-organic framework for efficient visible-light-driven conversion of CO<sub>2</sub> into CO, *ChemSusChem* 12 (2019) 2166–2170, <https://doi.org/10.1002/cssc.201900338>.
- [16] J.W. Maina, J.A. Schutz, L. Grundy, E. Des Ligneris, Z. Yi, L. Kong, C. Pozo-Gonzalo, M. Ionescu, L.F. Dumee, Inorganic nanoparticles/metal organic framework hybrid membrane reactors for efficient photocatalytic conversion of CO<sub>2</sub>, *ACS Appl. Mater. Interfaces* 9 (2017) 35010–35017, <https://doi.org/10.1021/acsaami.7b11150>.
- [17] Y. Xia, Z.H. Tian, T. Heil, A.Y. Meng, B. Cheng, S.W. Cao, J.G. Yu, M. Antonietti, Highly selective CO<sub>2</sub> capture and its direct photochemical conversion on ordered 2D/1D heterojunctions, *Joule* 3 (2019) 2792–2805, <https://doi.org/10.1016/j.joule.2019.08.011>.
- [18] M.P. Jiang, K.K. Huang, J.H. Liu, D. Wang, Y. Wang, X. Wang, Z.D. Li, X.Y. Wang, Z.B. Geng, X.Y. Hou, S.H. Feng, Magnetic-field-regulated TiO<sub>2</sub> {100} facets: a strategy for C-C coupling in CO<sub>2</sub> photocatalytic conversion, *Chem* 6 (2020) 2335–2346, <https://doi.org/10.1016/j.chempr.2020.06.033>.
- [19] K. Wang, J.B. Lu, Y. Lu, C.H. Lau, Y. Zheng, X.F. Fan, Unravelling the C-C coupling in CO<sub>2</sub> photocatalytic reduction with H<sub>2</sub>O on Au/TiO<sub>2-x</sub>: combination of plasmonic excitation and oxygen vacancy, *Appl. Catal. B Environ.* 292 (2021) 120147–120160, <https://doi.org/10.1016/j.apcatb.2021.120147>.
- [20] A.M. Appel, J.E. Bercau, A.B. Bocarsly, H. Dobbek, D.L. DuBois, M. Dupuis, J. G. Ferry, E. Fujita, R. Hille, P.J. Kenis, C.A. Kerfeld, R.H. Morris, C.H. Peden, A. R. Portis, S.W. Ragsdale, T.B. Rauchfuss, J.N. Reek, L.C. Seefeldt, R.K. Thauer, G. L. Waldrop, Frontiers, opportunities, and challenges in biochemical and chemical catalysis of CO<sub>2</sub> fixation, *Chem. Rev.* 113 (2013) 6621–6658, <https://doi.org/10.1021/cr300463y>.

- [21] Z.W. Wang, Y.Z. Shi, C. Liu, Y.Y. Kang, L. Wu,  $\text{Cu}^+-\text{Ti}^{3+}$  interface interaction mediated  $\text{CO}_2$  coordination model for controlling the selectivity of photocatalytic reduction  $\text{CO}_2$ , *Appl. Catal. B Environ.* 301 (2022) 120803–120813, <https://doi.org/10.1016/j.apcatb.2021.120803>.
- [22] H.J. Freund, M.W. Roberts, Surface-chemistry-of-carbon-dioxide, *Surf. Sci. Rep.* 25 (1996) 225–273, [https://doi.org/10.1016/S0167-5729\(96\)00007-6](https://doi.org/10.1016/S0167-5729(96)00007-6).
- [23] V.P. Indrakanti, J.D. Kubicki, H.H. Schobert, Photoinduced activation of  $\text{CO}_2$  on Ti-based heterogeneous catalysts: current state, chemical physics-based insights and outlook, *Energy Environ. Sci.* 2 (2009) 745–758, <https://doi.org/10.1039/b822176f>.
- [24] B.A. Rosen, A. Salehi-Khojin, M.R. Thorson, W. Zhu, D.T. Whipple, P.J. Kenis, R. I. Masel, Ionic liquid-mediated selective conversion of  $\text{CO}_2$  to CO at low overpotentials, *Science* 334 (2011) 643–644, <https://doi.org/10.1126/science.1209786>.
- [25] M. Gattrell, N. Gupta, A. Co, A review of the aqueous electrochemical reduction of  $\text{CO}_2$  to hydrocarbons at copper, *J. Electroanal. Chem.* 594 (2006) 1–19, <https://doi.org/10.1016/j.jelechem.2006.05.013>.
- [26] D.D. Zhu, J.L. Liu, S.Z. Qiao, Recent advances in inorganic heterogeneous electrocatalysts for reduction of carbon dioxide, *Adv. Mater.* 28 (2016) 3423–3452, <https://doi.org/10.1002/adma.201504766>.
- [27] X. Xiong, Y. Zhao, R. Shi, W. Yin, Y. Zhao, G.I.N. Waterhouse, T. Zhang, Selective photocatalytic  $\text{CO}_2$  reduction over Zn-based layered double hydroxides containing tri or tetravalent metals, *Sci. Bull.* 65 (2020) 987–994, <https://doi.org/10.1016/j.scib.2020.03.032>.
- [28] H. Zhong, M. Ghorbani-Asl, K.H. Ly, J. Zhang, J. Ge, M. Wang, Z. Liao, D. Makarov, E. Zschech, E. Brunner, I.M. Weidinger, J. Zhang, A.V. Krashenninnikov, S. Kaskel, R. Dong, X. Feng, Synergistic electroreduction of carbon dioxide to carbon monoxide on bimetallic layered conjugated metal-organic frameworks, *Nat. Commun.* 11 (2020) 1409–1419, <https://doi.org/10.1038/s41467-020-15141-y>.
- [29] J.D. Yi, D.H. Si, R. Xie, Q. Yin, M.D. Zhang, Q. Wu, G.L. Chai, Y.B. Huang, R. Cao, Conductive two-dimensional phthalocyanine-based metal-organic framework nanosheets for efficient electroreduction of  $\text{CO}_2$ , *Angew. Chem. Int. Ed.* 60 (2021) 17108–17114, <https://doi.org/10.1002/anie.202104564>.
- [30] Y.N. Gong, W. Zhong, Y. Li, Y. Qiu, L. Zheng, J. Jiang, H.L. Jiang, Regulating photocatalysis by spin-state manipulation of cobalt in covalent organic frameworks, *J. Am. Chem. Soc.* 142 (2020) 16723–16731, <https://doi.org/10.1021/jacs.0c07206>.
- [31] X. Wang, D. Yang, S. Zuo, H. Yang, Y. Zhou, Freestanding millimeter-scale porphyrin-based monoatomic layers with 0.28 nm thickness for  $\text{CO}_2$  electrocatalysis, *Angew. Chem. Int. Ed.* 59 (2020) 18954–18959, <https://doi.org/10.1002/anie.202006899>.
- [32] B. An, Z. Li, Y. Song, J.Z. Zhang, L.Z. Zeng, C. Wang, W.B. Lin, Cooperative copper centres in a metal-organic framework for selective conversion of  $\text{CO}_2$  to ethanol, *Nat. Catal.* 2 (2019) 709–717, <https://doi.org/10.1038/s41929-019-0308-5>.
- [33] L. Zhang, X.X. Li, Z.L. Lang, Y. Liu, J. Liu, L. Yuan, W.Y. Lu, Y.S. Xia, L.Z. Dong, D. Q. Yuan, Y.Q. Lan, Enhanced cuprophilic interactions in crystalline catalysts facilitate the highly selective electroreduction of  $\text{CO}_2$  to  $\text{CH}_4$ , *J. Am. Chem. Soc.* 143 (2021) 3808–3816, <https://doi.org/10.1021/jacs.0c11450>.
- [34] Y.N. Gong, J.H. Mei, J.W. Liu, H.H. Huang, J.H. Zhang, X.K. Li, D.C. Zhong, T. B. Lu, Manipulating metal oxidation state over ultrastable metal-organic frameworks for boosting photocatalysis, *Appl. Catal. B Environ.* 292 (2021) 120156–120165, <https://doi.org/10.1016/j.apcatb.2021.120156>.
- [35] D. Zhong, Z.J. Zhao, Q. Zhao, D. Cheng, B. Liu, G. Zhang, W. Deng, H. Dong, L. Zhang, J. Li, J. Li, J. Gong, Coupling of Cu(100) and (110) facets promotes carbon dioxide conversion to hydrocarbons and alcohols, *Angew. Chem. Int. Ed.* 60 (2021) 4879–4885, <https://doi.org/10.1002/anie.202015159>.
- [36] P. Huang, X. Huang, S.A. Pantovich, A.D. Carl, T.G. Fenton, C.A. Caputo, R. L. Grimm, A.I. Frenkel, G. Li, Selective  $\text{CO}_2$  reduction catalyzed by single cobalt sites on carbon nitride under visible-light irradiation, *J. Am. Chem. Soc.* 140 (2018) 16042–16047, <https://doi.org/10.1021/jacs.8b10380>.
- [37] C. Ye, J.-X. Li, Z.-J. Li, X.-B. Li, X.-B. Fan, L.-P. Zhang, B. Chen, C.-H. Tung, L.-Z. Wu, Enhanced driving force and charge separation efficiency of protonated  $\text{g-C}_3\text{N}_4$  for photocatalytic  $\text{O}_2$  evolution, *ACS Catal.* 5 (2015) 6973–6979, <https://doi.org/10.1021/acscatal.5b02185>.
- [38] J. Di, B. Lin, B. Tang, S. Guo, J. Zhou, Z. Liu, Engineering cocatalysts onto low-dimensional photocatalysts for  $\text{CO}_2$  reduction, *Small Struct.* 2 (2021), <https://doi.org/10.1002/sstr.202100046>.
- [39] D. Liu, S. Zhang, J. Wang, T. Peng, R. Li, Direct Z-scheme 2D/2D photocatalyst based on ultrathin  $\text{g-C}_3\text{N}_4$  and  $\text{WO}_3$  nanosheets for efficient visible-light-driven  $\text{H}_2$  generation, *ACS Appl. Mater. Interfaces* 11 (2019) 27913–27923, <https://doi.org/10.1021/acsaami.9b08329>.
- [40] B. Ma, G. Chen, C. Fave, L. Chen, R. Kuriki, K. Maeda, O. Ishitani, T.C. Lau, J. Bonin, M. Robert, Efficient visible-light-driven  $\text{CO}_2$  reduction by a cobalt molecular catalyst covalently linked to mesoporous carbon nitride, *J. Am. Chem. Soc.* 142 (2020) 6188–6195, <https://doi.org/10.1021/jacs.9b13930>.
- [41] X. Xiong, C. Mao, Z. Yang, Q. Zhang, G.I.N. Waterhouse, L. Gu, T. Zhang, Photocatalytic  $\text{CO}_2$  reduction to CO over Ni single atoms supported on defect-rich zirconia, *Adv. Energy Mater.* 10 (2020), <https://doi.org/10.1002/aenm.202002928>.
- [42] Y. Zhao, J. Wang, R. Pei, Micron-sized ultrathin metal-organic framework sheet, *J. Am. Chem. Soc.* 142 (2020) 10331–10336, <https://doi.org/10.1021/jacs.0c04442>.
- [43] M. Jahan, Q. Bao, K.P. Loh, Electrocatalytically active graphene-porphyrin MOF composite for oxygen reduction reaction, *J. Am. Chem. Soc.* 134 (2012) 6707–6713, <https://doi.org/10.1021/ja211433h>.
- [44] D.M. Chen, K.W. Wang, W.Z. Hong, R.L. Zong, W.Q. Yao, Y.F. Zhu, Visible light photoactivity enhancement via CuTCPP hybridized  $\text{g-C}_3\text{N}_4$  nanocomposite, *Appl. Catal. B Environ.* 166 (2015) 366–373, <https://doi.org/10.1016/j.apcatb.2014.11.050>.
- [45] J. Alberio, Y. Peng, H. Garcia, Photocatalytic  $\text{CO}_2$  reduction to  $\text{C}_2$ +Products, *ACS Catal.* 10 (2020) 5734–5749, <https://doi.org/10.1021/acscatal.0c00478>.
- [46] T. Su, Z.D. Hood, M. Naguib, L. Bai, S. Luo, C.M. Rouleau, I.N. Ivanov, H. Ji, Z. Qin, Z. Wu, 2D/2D heterojunction of  $\text{Ti}_3\text{C}_2/\text{g-C}_3\text{N}_4$  nanosheets for enhanced photocatalytic hydrogen evolution, *Nanoscale* 11 (2019) 8138–8149, <https://doi.org/10.1039/c9nr00168a>.
- [47] S. Mei, J. Gao, Y. Zhang, J. Yang, Y. Wu, X. Wang, R. Zhao, X. Zhai, C. Hao, R. Li, J. Yan, Enhanced visible light photocatalytic hydrogen evolution over porphyrin hybridized graphitic carbon nitride, *J. Colloid Interface Sci.* 506 (2017) 58–65, <https://doi.org/10.1016/j.jcis.2017.07.030>.
- [48] H. Sheng, H. Zhang, W. Song, H. Ji, W. Ma, C. Chen, J. Zhao, Activation of water in titanium dioxide photocatalysis by formation of surface hydrogen bonds: an in situ IR spectroscopy study, *Angew. Chem. Int. Ed.* 54 (2015) 5905–5909, <https://doi.org/10.1002/anie.201412035>.
- [49] S. Wang, B.Y. Guan, X.W. Lou, Rationally designed hierarchical N-doped carbon@ $\text{NiCo}_2\text{O}_4$  double-shelled nanoboxes for enhanced visible light  $\text{CO}_2$  reduction, *Energy Environ. Sci.* 11 (2018) 306–310, <https://doi.org/10.1039/c7ee02934a>.
- [50] H.H. Liu, F. Zhang, H.F. Wang, J.R. Xue, Y.M. Guo, Q.Z. Qian, G.Q. Zhang, Oxygen vacancy engineered unsaturated coordination in cobalt carbonate hydroxide nanowires enables highly selective photocatalytic  $\text{CO}_2$  reduction, *Energy Environ. Sci.* 14 (2021) 5339–5346, <https://doi.org/10.1039/d1ee01397a>.
- [51] P. Sharrock, M. Melnik, Copper(II) acetates: from dimer to monomer, *J. Chem.* 63 (1985) 52–56, <https://doi.org/10.1139/v85-009>.
- [52] S.P. Greiner, D.L. Rowlands, R.W. Kreilick, EPR, ENDOR, Study of selected porphyrin-copper and phthalocyanine-copper complexes, *J. Phys. Chem.* 96 (1992) 9132–9139, <https://doi.org/10.1021/j100202a012>.
- [53] H.U. Guedel, A. Stebler, A. Furrer, Direct observation of singlet-triplet separation in dimeric copper(II) acetate by neutron inelastic scattering spectroscopy, *Inorg. Chem.* 18 (1979) 1021–1023, <https://doi.org/10.1021/ic50194a029>.
- [54] E.I. Solomon, D.E. Heppner, E.M. Johnston, J.W. Ginsbach, J. Cirera, M. Qayyum, M.T. Kieber-Emmons, C.H. Kjaergaard, R.G. Hadt, L. Tian, Copper active sites in biology, *Chem. Rev.* 114 (2014) 3659–3853, <https://doi.org/10.1021/cr400327t>.
- [55] A. Bencini, D. Gatteschi, *Electron Paramagnetic Resonance of Exchange Coupled Systems*, Springer-Verlag, Berlin Heidelberg, 1990.
- [56] C. Sigwart, P. Hemmeric, J.T. Spence, A binuclear mixed-valence copper acetate complex as a model for copper-copper interaction in enzymes, *Inorg. Chem.* 7 (1968) 2545–2548, <https://doi.org/10.1021/ic50070a015>.
- [57] R.I. Saylor, B.M. Hunter, W. Fu, H.B. Gray, R.D. Britt, EPR spectroscopy of iron- and nickel-doped [ZnAl]-layered double hydroxides: modeling active sites in heterogeneous water oxidation catalysts, *J. Am. Chem. Soc.* 142 (2020) 1838–1845, <https://doi.org/10.1021/jacs.9b10273>.
- [58] T. Wu, C. Zhu, D. Han, Z. Kang, L. Niu, Highly selective conversion of  $\text{CO}_2$  to  $\text{C}_2\text{H}_6$  on graphene modified chlorophyll Cu through multi-electron process for artificial photosynthesis, *Nanoscale* 11 (2019) 22980–22988, <https://doi.org/10.1039/c9nr07824j>.
- [59] S. Sorcar, J. Thompson, Y. Hwang, Y.H. Park, T. Majima, C.A. Grimes, J.R. Durrant, S.-I. In, High-rate solar-light photocatalysis of  $\text{CO}_2$  to fuel: controllable transformation from C1 to C2 products, *Energy Environ. Sci.* 11 (2018) 3183–3193, <https://doi.org/10.1039/c8ee00983j>.
- [60] N.X. Li, B.B. Wang, Y.T. Si, F. Xue, J.C. Zhou, Y.J. Lu, M.C. Liu, Toward high-value hydrocarbon generation by photocatalytic reduction of  $\text{CO}_2$  in water vapor, *ACS Catal.* 9 (2019) 5590–5602, <https://doi.org/10.1021/acscatal.9b00223>.
- [61] J.B. Sambur, T.Y. Chen, E. Choudhary, G. Chen, E.J. Nissen, E.M. Thomas, N. Zou, P. Chen, Sub-particle reaction and photocurrent mapping to optimize catalyst-modified photoanodes, *Nature* 530 (2016) 77–80, <https://doi.org/10.1038/nature16534>.
- [62] N.D. Nielsen, T.E.L. Smitshuysen, C.D. Damsgaard, A.D. Jensen, J.M. Christensen, Characterization of oxide-supported Cu by infrared measurements on adsorbed CO, *Surf. Sci.* 703 (2021) 121725–121739, <https://doi.org/10.1016/j.susc.2020.121725>.
- [63] Z. Liu, A. Rittermeier, M. Becker, K. Kahler, E. Löffler, M. Muhler, High-pressure CO adsorption on Cu-based catalysts: Zn-induced formation of strongly bound CO monitored by ATR-IR spectroscopy, *Langmuir* 27 (2011) 4728–4733, <https://doi.org/10.1021/la2000766>.
- [64] J.J. Gutiérrez-Sevillano, J.M. Vicent-Luna, D. Dubbeldam, S. Calero, Molecular mechanisms for adsorption in Cu-BTC metal organic framework, *J. Phys. Chem. C* 117 (2013) 11357–11366, <https://doi.org/10.1021/jp401017u>.
- [65] C.H. Lim, A.M. Holder, C.B. Musgrave, Mechanism of homogeneous reduction of  $\text{CO}_2$  by pyridine: proton relay in aqueous solvent and aromatic stabilization, *J. Am. Chem. Soc.* 135 (2013) 142–154, <https://doi.org/10.1021/ja3064809>.
- [66] W. Zhang, C. Huang, J. Zhu, Q. Zhou, R. Yu, Y. Wang, P. An, J. Zhang, M. Qiu, L. Zhou, L. Mai, Z. Yi, Y. Yu, Dynamic restructuring of coordinatively unsaturated Cu paddle wheel clusters to boost electrochemical  $\text{CO}_2$  reduction to hydrocarbons, *10.1002/anie.202112116*, *Angew. Chem. Int. Ed.* (2021), <https://doi.org/10.1002/anie.202112116>.